Talanta 294 (2025) 128273

Contents lists available at ScienceDirect

Talanta

journal homepage: www.elsevier.com/locate/talanta

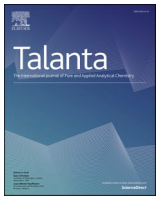

Unlocking the power of chirality: Surface nanoarchitectonics of modified halloysite nanotubes for enantioselective recognition

Malinee Niamlaem [a,1], Sara Grecchi [a,1], Punjapol Matthayom [b], Chompunuch Warakulwit [b], Daniela Maggioni [a], Serena Arnaboldi [a,*]

[a] Università degli Studi di Milano, Dipartimento di Chimica, Via Golgi 19, 20133, Milano, Italy
[b] Department of Chemistry, Faculty of Science and Center for Advanced Studies in Nanotechnology for Chemical, Food, and Agricultural Industries, Kasetsart University Institute for Advanced Studies, Kasetsart University, Bangkok, 10900, Thailand

ARTICLE INFO

Handling Editor: Prof Agata Michalska

Keywords:
Halloysite nanotubes
Inherently chiral oligomers
Chirality
Enantioselective recognition

ABSTRACT

Developing cost-effective electrode materials with high performance for enantioselective recognition is rapidly gaining attention. In this work, we harness the unique physicochemical properties of halloysite nanotubes (HNTs) as innovative electrode platforms for chiral discrimination. We functionalized HNTs with an enantiopure oligomer based on thiophene units via chemical oligomerization using $FeCl_3$ as an oxidizing agent. The successful functionalization of the HNTs with the oligomer was further confirmed by both solid state ^{13}C NMR and zeta potential studies (from -20.0 ± 1.5 mV to -12.4 ± 3.0 mV after modification). The resulting composite materials (oligo-(*S*)- and oligo-(*R*)- modified HNTs) demonstrated remarkable enantioselective recognition capabilities in terms of peak potential values (560–650 mV) when testing the enantiomers of DOPA, a chiral drug of pharmaceutical interest. These findings highlight the potential of HNT-based modified electrodes as a novel class of chiral electrochemical sensors, paving the way for advanced applications in enantioselective analysis.

1. Introduction

Highly efficient enantioselective recognition of chiral molecules is fundamental in multiple research fields [1,2]. For example, in the pharmaceutical industry, most active substances are chiral; in particular, only one of the enantiomers is of medical importance [3]. As is well known, the antipodes of a chiral analyte are non-superimposable mirror image molecules that exhibit significant differences in chemical and biological activity. Developing enantioselective analytical methods is paramount since both enantiomers present similar physicochemical properties. Different and sophisticated analytical methods have been developed, from chiral chromatography [4,5] to enantioselective nuclear magnetic resonance spectroscopy [6], eventhough, most of these require expensive instrumentation and rather time-consuming manipulation. In this context, electrochemical methods have gained considerable attention due to their simplicity, high sensitivity, and low cost [7–9]. Since enantiorecognition occurs exclusively in a chiral environment and electrochemistry is an interfacial process, asymmetrically modified surfaces are required. Different and complex chemically modified electrodes have been studied, from molecularly imprinted metals to cyclodextrins and chiral metal-organic frameworks [10–15]. Nevertheless, the enantiodiscrimination is based on a difference in current intensity between the signals of the two antipodes of a chiral probe, which limits the use of these modified electrodes for the in-situ analysis of enantiomeric mixtures.

In recent years, inherently chiral oligomers, such as the 2,2′-bis(2,2′-bithiophene-5-yl)-3,3′-bibenzothiophene (BT_2T_4) have been studied, exhibiting excellent high electroactivity and outstanding enantioselectivity [16–19], in terms of thermodynamic differences between the antipodes of a chiral probe. In this type of π-conjugated polymers, where the stereogenic and electroactive elements coincide within the polymeric backbone, enantiorecognition occurs due to the induction of diastereomeric interactions between the oligomeric layer and the enantiomers of an electroactive analyte. Building upon previous successes in enantioselective recognition, we aim to further enhance the performance of chiral electrodes. Our prior work demonstrated the effective

This article is part of a special issue entitled: Electroanalysis published in Talanta.

* Corresponding author.
E-mail address: serena.arnaboldi@unimi.it (S. Arnaboldi).

[1] These authors contributed equally.

https://doi.org/10.1016/j.talanta.2025.128273
Received 28 November 2024; Received in revised form 28 April 2025; Accepted 3 May 2025
Available online 5 May 2025

discrimination of enantiomers using oligo-(*R*)- and oligo-(*S*)-BT_2T_4 modified electrodes, particularly for probes related to the tyrosin biological catecholamine pathway [19]. To amplify these enantiorecognition capabilities, we now turn our attention to high surface area substrates. By depositing the oligomeric materials on such substrates, we can create a sophisticated chiral environment that mimics bulk enantiorecognition, potentially leading to even greater selectivity and efficiency. This approach holds promise for advancing the field of chiral electrochemistry and enabling new applications in enantioselective analysis and separation.

In this context, halloysite nanotubes (HNTs), a cost-effective mineral clay of the kaolin group, with a hollow tubular structure composed of aluminosilicate layers with external tetrahedral silica (Si–O–Si) and internal octahedral alumina (Al–OH) sheets, is presented as a promising high surface area substrate. The length of these nanotubes is in the micrometer range, with an outer and inner diameter between 50 and 100 nm and 10–60 nm, respectively. HNTs have attracted considerable attention due to their unique chemical and physical properties, such as good biocompatibility, opposite charge structure between the inner and outer surface, low cost, surface reactivity, hollow cavities, easy dispensability, and high chemical stability [20–22]. These excellent properties enable the use of HNTs in different applications, such as drug delivery [23], CO_2 adsorption [24], environmental remediation [25], and energy storage [26].

In this work, the negative outer surface of HNTs was modified with the enantiomers of BT_2T_4 oligomers, acting as chiral environment, to electrochemically recognize the antipodes of 3,4-dihydroxyphenylalanine (DOPA). A thermodynamic peak-to-peak separation between the voltammetric signals of the DOPA enantiomers was achieved due to the formation of matching and mismatching configurations between the inherently chiral oligomer and the antipode of the chiral analyte. This study opens the way to design a novel type of advanced high surface area materials in bulk enantioselective processes for future applications in enantioseparation [27,28], asymmetric synthesis [29–31], or electroanalysis.

2. Experimental sections

2.1. Materials and reagents

Halloysite nanotubes (HNTs), 1-butyl-3-methylimidazolium bis(trifluoromethylsulfonyl)imide (BMIM/TFSI), and D-, L-3,4-dihydroxyphenylalanine (D-, L-DOPA) were purchased from Sigma-Aldrich while ferric chloride hexahydrate ($FeCl_3.6H_2O$) from Carlo Erba Reagents. Analytical grade of acetonitrile (ACN) was purchased from Honeywell Riedel-de-Haën™. All chemicals and solvents were used without further purification. Enantiopure inherently chiral monomers, (*S*)- or (*R*)-2,2′-bis[2-(5,2′-bithienyl)]3,3′-bithianaphthene ((*S*)-BT_2T_4 or (*R*)-BT_2T_4) were synthesized and separated through chiral HPLC in our laboratory following a published methodology [32].

2.2. Chemical oligomerization of enantiopure BT_2T_4 on HNTs (named oligo-(S)-BT_2T_4@HNTs or oligo-(R)-BT_2T_4@HNTs)

The oligo-(*S*)- and oligo-(*R*)-BT_2T_4@HNTs materials were prepared via chemical oligomerization (Fig. 1-a). Briefly, 30 mg of HNTs was

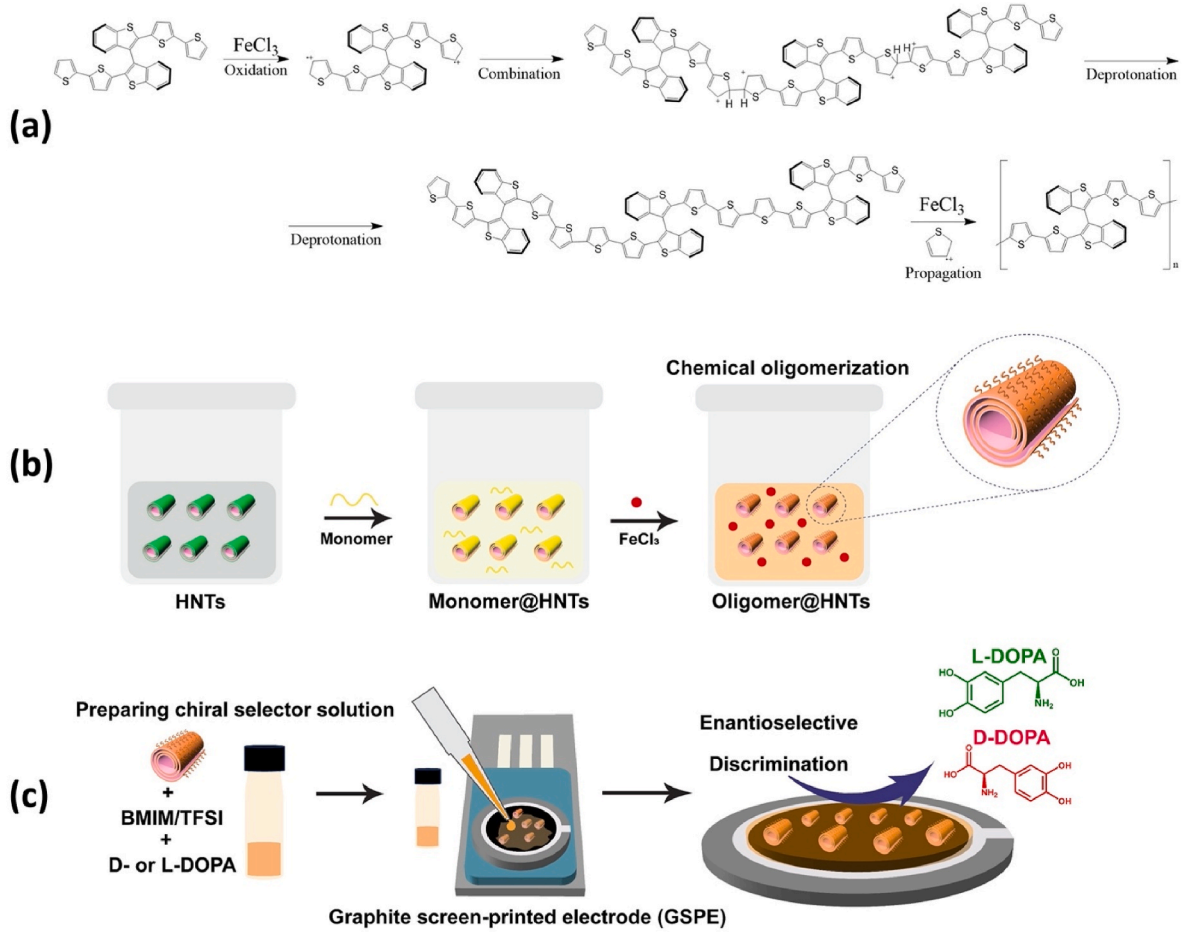

Fig. 1. Schematic illustration of (a) chemical oligomerization of BT_2T_4, (b) preparation of modified HNTs, and (c) steps for preparing the enantioselective electrode surface.

dispersed in 30 mL of ACN. Afterward the solution was kept under sonication for 15 min and then stirred at room temperature for 15 min to produce a homogenous dispersion. Then, 0.085 mM of enantiopure BT_2T_4 was mixed with the HNTs solution under continuous stirring for 1 h at room temperature to better incorporate the inherently chiral monomer onto the surface of HNTs. 0.013 M of $FeCl_3$, acting as an oxidant, was rapidly added to the mixture solution under constant stirring allowing reaction running for 24 h, at room temperature (Fig. 1-b). After 24 h, the obtained materials were then collected and washed five times with ACN via centrifugation (6000 rpm for 10 min, Centrifuge-4226). The sample was then dried in an oven at 40 °C for 1 h to remove the excess solvent. The kinetic of BT_2T_4 oligomerization on HNTs was followed via ultraviolet and visible (UV–vis) spectroscopy with a UV-1800 spectrophotometer (SHIMADZU). 500 μL samples at different oligomerization times were transferred into a quartz cuvette and diluted with 500 μL of ACN. The UV–vis spectra of the solution were then measured in a wavelength range from 250 nm to 1100 nm.

2.3. Characterizations

The pristine HNTs and the obtained oligo-(*S*)- and oligo-(*R*)-BT_2T_4@HNTs samples were analyzed by different physicochemical methods. Fourier transform infrared (FTIR) measurements were performed with a Jasco spectrometer (FT/IR-4600) in a wavenumber range of 500–4000 cm^{-1} and 500 scans to confirm the nature of the deposited materials. Thermal gravimetric analysis (TGA) was carried out by using TGA-8000 (PerkinElmer) from 30 to 800 °C under nitrogen flow (20 mL/min) with a heating rate of 10 °C/min. The size and morphology of the corresponding materials were characterized utilizing field emission scanning and transmission electron microscopy (FE-SEM and FE-TEM) on JEOL JSM-7600F and JEOL JEM-3100F at 1 and 300 kV, respectively. For TEM analysis, samples were dispersed in ethanol before transferring onto a copper grid. ^{13}C solid-state NMR spectra were obtained on a JEOL ECA400 spectrometer at 400 MHz (spinning rate, 15 kHz) using a cross-polarization sequence with a 5 ms contact time and a 5 s relaxation delay; the chemical shifts were referenced to TMS, kaolinite and H_3PO_4, respectively. Zeta potential of bare HNTs and HNTs modified with oligo-*Rac*-BT_2T_4 were measured with a Zetasizer Nano series (Malvern Instruments).

2.4. Enantiorecognition tests

The potentiodynamic characterization of the chiral probes was carried out with an AUTOLAB potentiostat-galvanostat PGSTAT101 (Metrohm Lab Instruments) connected to a personal computer. A plastic screen-printed three-electrode system (SPE), composed of graphite, silver, and platinum, acting as working, pseudo reference, and counter electrodes was used, respectively. The analysis solution was formed by mixing 0.6 mg of modified HNTs and 200 μL of BMIM/TFSI ionic liquid containing 6 mM of D-DOPA or L-DOPA as chiral analytes. The same procedure was used to evaluate the linear dynamic range (from 1 mM to 8 mM). The samples were then placed under sonication for at least 2 h to obtain homogenous dispersion. After that, 0.5 μL of the mixture solution was drop-casted on the surface of the SPE (see Fig. 1-c). The voltammograms were recorded in a potential range from 0 to 1.8 V vs. Ag° at a potential scan rate of 50 mV/s. In addition, the reproducibility and stability of the modified electrodes were verified by carrying out all the experiments three times.

2.5. Encapsulation efficiency and drug loading determinations

The encapsulation efficiency (EE) and drug loading (DL) of DOPA into the oligo-(*R*)-BT_2T_4@HNTs were determined using both an indirect and a direct method.

Indirect Method: A known amount of the DOPA-loaded HNTs was dispersed in buffer solution pH 4. The suspension was then subjected to centrifugation to separate the HNTs from the solution containing the free DOPA. The concentration of free DOPA in the supernatant was quantified using UV–vis spectroscopy. A calibration curve was prepared using known concentrations of DOPA in the same solvent. The absorbance of the supernatant was measured at the appropriate wavelength, and the concentration of free DOPA was determined from the calibration curve.

Direct Method: A known amount of the DOPA-loaded HNTs was smashed and added to a buffer pH 4 solution to completely allow the release of the encapsulated DOPA. The total amount of DOPA in the solution was quantified using UV–vis spectroscopy, following the same procedure and calibration curve as described for the indirect method.

The encapsulation efficiency (EE) and drug loading (DL) were calculated using the following equations:

$$\text{EE}\ (\%) = (\text{Amount of DOPA measured after smashing and dissolution}) / (\text{Total amount of DOPA initially added}) * 100$$

$$\text{DL}\ (\%) = (\text{Amount of DOPA measured after smashing and dissolution}) / (\text{Total weight of HNTs with DOPA}) * 100$$

All measurements were performed in triplicate for both methods, and the results were averaged.

2.6. Enantioselective release study of D- and L-DOPA from oligomer-modified HNTs

A known amount of D-DOPA-loaded or L-DOPA-loaded HNTs was suspended in 5 mL of the release medium (buffer pH 4) and placed inside a dialysis bag. The dialysis bag had a molecular weight cutoff (MWCO) of 3.5 kDa, which allows the passage of DOPA while retaining the HNTs. The dialysis bag was then immersed in a larger volume of the release medium in a cell under constant stirring. At predetermined time intervals (0.5, 1, 2, 4, 8, 12, 24, 48 h), 1 mL of the release medium was withdrawn from the receiving compartment. The withdrawn volume was immediately replaced with an equal volume of fresh release medium to maintain a constant volume. The concentration of D-DOPA and L-DOPA in the collected samples was determined using HPLC. The samples were injected into a C18, 4.6 × 150 mm, 5 μm particle size, using a mobile phase consisting of 20 mM phosphate buffer, pH 2.5–3.0, with 0.1 % acetic acid and methanol (90:10) at a flow rate of 1.0 mL/min. The detection wavelength was set at 280 nm. Calibration curves for D-DOPA and L-DOPA were prepared using standard solutions of known concentrations in the release medium. The concentrations of D-DOPA and L-DOPA in the samples were determined by comparing the peak areas to the respective calibration curves. The cumulative amount of D-DOPA and L-DOPA released at each time point was calculated and expressed as a percentage of the total drug loaded, using the following equation:

$$\text{Cumulative Release}\ (\%) = (\text{Amount of DOPA released at time t} / \text{Total amount of DOPA loaded}) * 100$$

Release profiles (cumulative release vs. time) were plotted for D-DOPA and L-DOPA from both oligo-(*S*)-BT_2T_4@HNTs and oligo-(*R*)-BT_2T_4@HNTs.

The initial burst release (defined as the release within the first 0.5 h) and the release rate (calculated from the slope of the linear portion of the release curve) were determined. The data was fitted to first-order release model to investigate the mechanism.

3. Results and discussion

Although the oligomerization is commonly performed through electrochemistry on the electrodic surfaces, this leads to the immobilization of the chiral selector at the electrochemical interface, which represents, in some applications, a technical limitation. Therefore, the

possible chemical oligomerization of the racemic mixture of BT_2T_4 monomer onto the surface of HNTs was performed in the presence of a strong oxidant agent ($FeCl_3$). Under these conditions, the well-established oligomerization mechanism of π-conjugated materials occurs (Fig. 1-a) [33,34]. Briefly, during the oxidation of BT_2T_4, the formed radical cations dimerize at the α-positions of the thiophene groups, which, after proton elimination, produce the neutral dimers. Due to the high thermodynamic driving force of the $FeCl_3$, the subsequent oxidation of the dimers takes place, which undergoes a series of coupling steps. Once enough oligomeric structures are formed, the nucleation and growth of short-chain polymeric structures are deposited via electrostatic interactions. Hence, it is possible to assume that the nucleation and growth of long-chain oligomeric structures can occur at the negatively charged outer surface of HNTs. To corroborate this hypothesis, we evaluate the kinetics of oligomerization of the racemic BT_2T_4 monomer in a HNTs/ACN suspension in the presence of $FeCl_3$ through UV–vis spectroscopy (Fig. 2). As can be seen, the bare HNTs suspension does not exhibit any evident absorption band in the wavelength range of work (Fig. 2a-black line). However, in the presence of the racemic monomer, a band around 400 nm appeared, which can be attributed to the π-π* electron transition (see Fig. 2a-blue line) of the

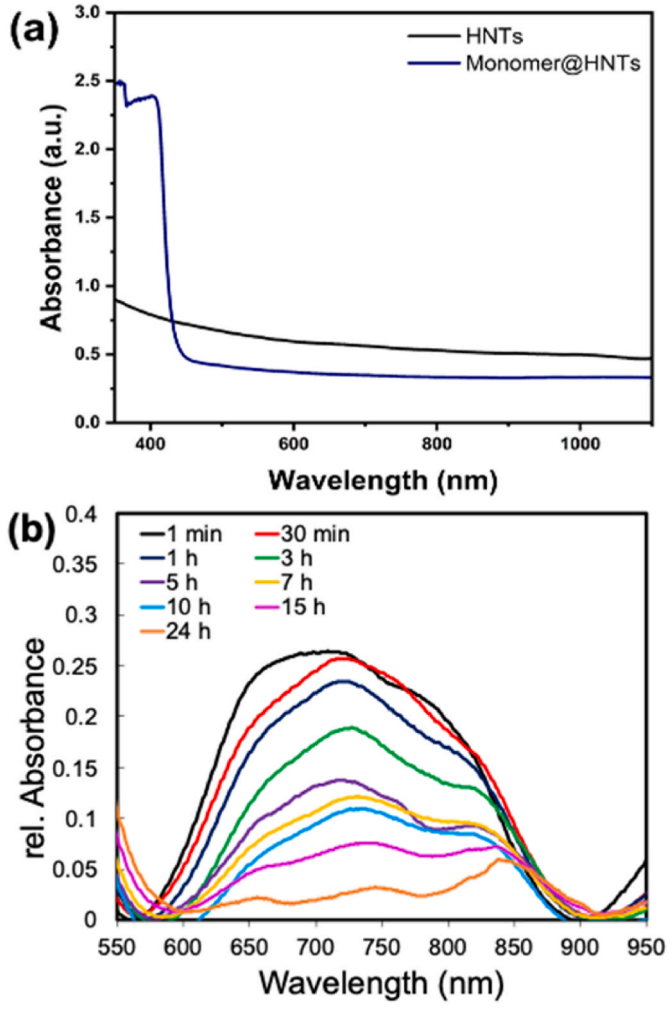

Fig. 2. UV–vis spectra of (a) bare HNTs (black line) and HNTs with adsorbed racemic BT_2T_4 monomer (blue line) in acetonitrile solution before chemical oligomerization, and (b) UV–vis spectra showing the evolution of BT_2T_4 chemical oligomerization in acetonitrile solution in the presence of HNTs at room temperature over 24 h (baseline corrected). (For interpretation of the references to colour in this figure legend, the reader is referred to the Web version of this article.)

BT_2T_4. Upon addition of $FeCl_3$, multiple absorption bands in a range between 550 and 900 nm appear, indicating the rapid formation of the radical-cation (Fig. 2b-black line). In particular, the absorption bands between 600 and 900 nm are attributed to charged species associated with the conducting state of π-conjugated oligomeric films. As the oligomerization time increases, all the absorption bands combine to form more conjugated polaronic and bipolaronic states. The UV–vis spectra in Fig. 2b reveal a decrease in absorbance in the 600–800 nm region as the oligomerization of BT_2T_4 progresses over 24 h. This observation can be attributed to conformational changes in the growing oligomers. Initially, the shorter oligomers may adopt a more coiled or twisted conformation, limiting the extent of π-conjugation. However, as the oligomers grow longer, they can undergo a transition to a more planar conformation, extending the conjugation length and leading to a red shift in the absorption bands. This red shift is evidenced by the emergence of a new band at longer wavelengths (after 800 nm) as the reaction proceeds. The extended conjugation in the more planar conformation results in a decrease in the energy gap between electronic states, causing the absorption to shift towards lower energies and longer wavelengths. This phenomenon is consistent with the well-documented trend of red-shifting absorption bands with increasing conjugation length in various conjugated polymers [32]. Since during this type of oligomerization, the produced material is in its cationic state, the negatively charged outer surface of HNTs acts as a counter ion to keep the electroneutrality of the system. Hence, as stated above, the oligomers' nucleation and growth may occur at the surface of the HNTs. To provide evidence of the chemical modification, we compared the IR spectrum of the bare HNTs and the oligo-*Rac*-BT_2T_4@HNTs composite (see Fig. S1 (a-c)). As it can be seen, the IR spectrum of the pristine HNTs present absorption bands at 3690 cm^{-1} and 3627 cm^{-1} attributed to the O–H groups in the inner and the outer surface of HNTs, respectively. In addition, a band at 1118 cm^{-1} assigned to the Si–O stretching and multiple signals at 1076 cm^{-1}, 1037 cm^{-1}, 910 cm^{-1}, 647-683 cm^{-1}, and 529 cm^{-1} characterized the vibration of Si–O–Si and O–Si, bending vibration of Al–OH, symmetrical vibrational stretching of Si–O and deformation of Al–O–Si groups, respectively [35–39]. After the chemical oligomerization of BT_2T_4 the main absorption bands of HNTs remain but some differences can be appreciated in the ranges between 3000 and 3500 cm^{-1} (Fig. S1 (b)) and 3000-1500 cm^{-1} (Fig. S1 (c)), in particular a small broad band appears between 3050 and 3100 cm^{-1} which is attributed to the region of such oligothiophene-based oligomers (Fig. S1 (b))[40].

Solid-state NMR spectroscopy was employed to further confirm the successful modification of the HNTs. The ^{13}C solid-state NMR spectra of the pristine HNTs and the modified HNTs are shown in Figure S1 (d-e). The pristine HNTs exhibits no signals in the ^{13}C spectrum coherent with the fact that halloysites are mainly constituted of Si and O (Fig. S1 (d)). In contrast, the spectrum of the modified HNTs shows additional signals in the range of 120–150 ppm, which can be attributed to the aromatic carbons of unsaturated species decorating HNTs (Fig. S1 (e)). Such results confirm the presence of the oligomer on the surface of the HNTs [41].

The outer layer modification was corroborated by comparing the surface morphology of the pristine HNTs and the oligo-(*S*) and oligo-(*R*)-BT_2T_4@HNTs composites (Fig. 3-left, Fig. 3-middle and Fig. 3-right). As expected, the SEM images of the bare HNTs show a relatively smooth surface with the typical nanotube structure (Fig. 3a-left panel), whereas, after chemical modification, the HNTs exhibit a rough granular surface characteristic for the deposit of the enantiomers of BT_2T_4 (Fig. 3b and 3c-left panel). The low and high magnification TEM of the pristine HNTs show the characteristic hollow nanotube structure with a smooth surface (Fig. 3a-middle and right panels) and an outer diameter of 64.2 ± 28.4 nm. Once again, after BT_2T_4 oligomerization, the TEM images present a rough granular surface indicating the deposit of the chiral oligomer at the HNTs surfaces (see Fig. 3b-3c-middle and right panels). Interestingly, a significant difference in the outer diameter of the oligo-(*S*)-

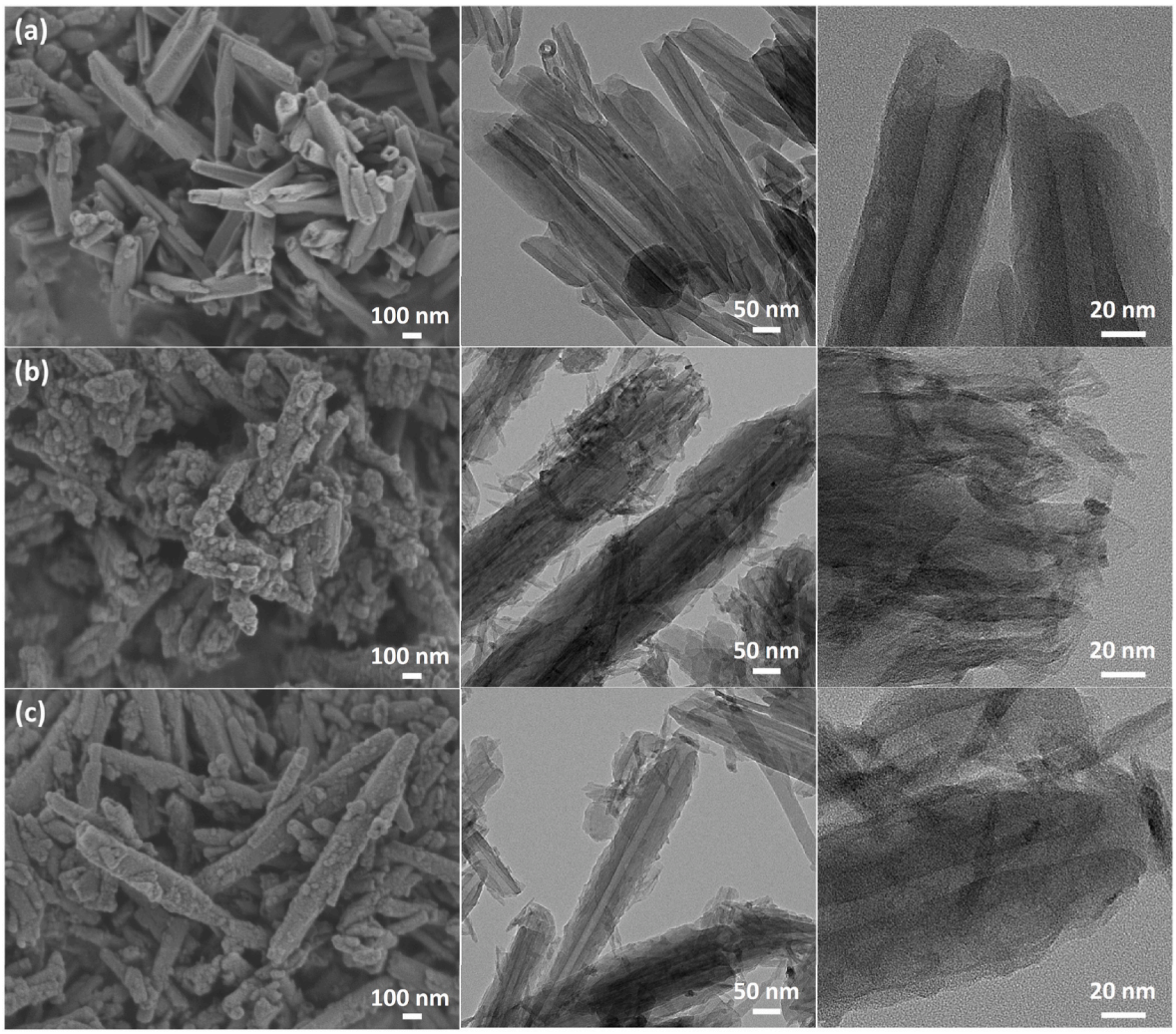

Fig. 3. SEM (left), low-magnification TEM (middle), and high-magnification TEM (right) images of the pristine HNTs and modified HNTs materials. (a) bare HNTs, (b) oligo-(*S*)-BT_2T_4@HNTs and oligo-(*R*)-BT_2T_4@HNTs

BT_2T_4@HNTs (113.7 nm ± 41.6) and the oligo-(*R*)-BT_2T_4@HNTs (175.1 nm ± 102.4) has been observed, which could be attributed to several factors, such as variations in the oligomer conformation on the HNT surface, the influence of chirality on the oligomerization process, or inherent heterogeneity in the starting HNTs. While the exact reason for this difference requires further investigation, our preliminary results suggest that it does not significantly affect the enantioselectivity of the modified HNTs towards DOPA. Both types of HNTs exhibit comparable peak-to-peak separation in the CV curves, indicating similar enantiorecognition capabilities.

TEM analysis reveals a helical-like chain growth orientation onto the surface of HNTs. This was corroborated by comparing the morphology of the oligo-BT_2T_4 in the absence of HNTs (Fig. S2), where a granular growth with no apparent well-defined structures was obtained. It is possible to assume that the inherent chiral oligomer's handedness guides the growth's orientation.

The composition and the thermal stability of the HNTs composite materials were evaluated via thermogravimetric analysis (TGA) (see Fig. S3). The weight and related derivative curves of bare HNTs, oligo-(*S*)- and oligo-(*R*)-BT_2T_4@HNTs exhibit a first weight loss below 100 °C and at 170 °C corresponding to the desorption of water at the outer and inner layers of the HNTs. The significant weight loss peak observed at ~515 °C is associated with the dehydroxylation of structural aluminol groups of HNTs [36]; nonetheless, a slight degradation of the HNTs structure can take place between 400 and 600 °C. However, the residual pristine HNTs sample (83.4 %) is higher than the one of the oligo-(*S*)-BT_2T_4@HNTs (80.0 %) and oligo-(*R*)-BT_2T_4@HNTs (81.1 %), which is attributed to the decomposition of the enantiopure oligomers (~1.5 %). In addition, zeta potential and size distribution of the HNTs sample before and after modification with oligo-BT_2T_4 were investigated, as shown in Fig. S4. The hydrodynamic average size increased from 282 ± 116 nm to 2125 ± 549 nm. These results are coherent with the zeta potential values. Pristine HNT has a negative zeta potential of −20.0 ± 1.5 mV and, after modification of −12.4 ± 3.0 mV, confirming the halloysite functionalization. pH measured by maintaining constant the ionic strength of the medium resulted in 7.9 for bare halloysites and 4.2 for the ones modified with the oligomer; the negative zeta potential of the unmodified HNTs indicates that the surface carries a negative charge. This is typical for halloysite, which has a structure that often leads to a net negative charge in aqueous solutions. This negative charge is usually attributed to the presence of hydroxyl groups (OH^-) on the surface. After modification with oligo-BT_2T_4, the zeta potential becomes less negative. This suggests that the modification process neutralizes some of the HNT surface's negative charges. The oligo-BT_2T_4 likely interacts with the HNT surface, potentially through electrostatic interactions or other chemical bonding, and this interaction reduces the overall negative charge.

Following the characterization of the oligo-BT_2T_4-modified HNTs, their enantiorecognition capabilities were assessed potentiodynamically on graphite SPEs. This involved independent testing of 0.5 μL

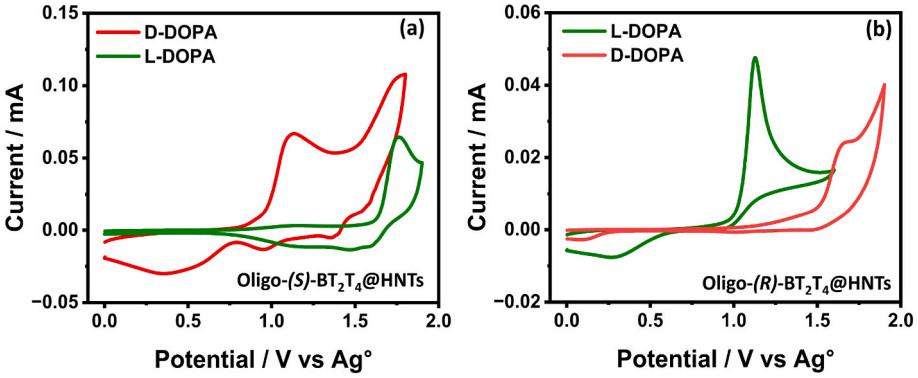

Fig. 4. CV curves of 6 mM D-DOPA (red line) or L-DOPA (green line) of (a) oligo-(*S*)-BT_2T_4@HNTs/GSPE and (b) oligo-(*R*)-BT_2T_4@HNTs/GSPE in BMIM/TFSI ionic liquid on SPEs at 0.05 V/s potential scan rate. (For interpretation of the references to colour in this figure legend, the reader is referred to the Web version of this article.)

composites in a BMIM/TFSI ionic liquid suspension containing 6 mM of either D- or L-DOPA, serving as model analytes (Fig. 4). Further experiments were conducted to evaluate the linear dynamic range by varying the D- and L-DOPA concentrations from 1 mM to 8 mM (Fig. S5).

As it can be seen, since the electroactive polymers are in suspension, the charge/discharge process of the oligomers is rather neglectable for both enantiomers oligo-(*S*)- and oligo-(*R*)-BT_2T_4@HNTs (Fig. S6). However, in the presence of DOPA antipodes, the voltammetric response changes due to the possible formation of diastereomeric interactions between the probes and the enantiopure composites. When using the oligo-(*S*)-BT_2T_4@HNTs electrode, the oxidation of D-DOPA appears at lower anodic potential values (around 1.13 V vs. Ag°) whereas for the L-DOPA a shift toward higher anodic potentials (1.76 V vs. Ag°) was obtained (Fig. 4a). The significant peak-to-peak separation (approximately 600 mV) observed in the cyclic voltammograms demonstrates the preferential interaction of the oligo-(*S*)-BT_2T_4@HNTs composite with D-DOPA. This selectivity arises from a matching diastereomeric interaction between the (*S*)-oligomer and the D-chiral probe, as corroborated by the reproducibility test (Fig. S7). Similarly, the composite with the opposite (*R*) configuration exhibits a comparable peak-to-peak separation, favorably oxidizing L-DOPA (1.13 V vs. Ag°). These results confirm that the modified oligo-(*S*)- and oligo-(*R*)-BT_2T_4@HNTs composites can selectively enhance or inhibit the oxidation of DOPA enantiomers, respectively. The use of HNTs as a support for the chiral selector effectively mimics an asymmetric environment, enabling bulk-type recognition and amplifying the enantioselectivity. LOD (3.3 mM) and sensitivity (0.098 mA/mM) calculations have shown that the HNT-based modified electrodes exhibit a good sensitivity for DOPA detection, although they may not be the most sensitive among the reported methods. The higher sensitivity compared to some other electrodes could be attributed to the unique properties of HNTs, such as their high surface area and ability to enhance the electrochemical signal. However, the LOD of the HNTs-based modified electrode is significantly higher than the LODs reported for most other electrochemical methods for DOPA detection [19,42–48]. This suggests that the sensitivity of the method might need improvement to be comparable to other approaches. The relatively high LOD of the method could be attributed to several factors, such as the high background current from the HNTs, the low concentration of the chiral selector on the electrode surface, or the use of cyclic voltammetry, which is generally less sensitive than other techniques like differential pulse or square wave voltammetry. Table S1 compares different materials for the enantioselective discrimination of DOPA, showing that approaches based on potential differences generally exhibit greater discrimination than those based on current intensity. This difference in performance may reflect the thermodynamics of the interactions between the chiral selector and the probe enantiomers. Potential-based methods, like the HNT system in this work, demonstrate larger peak-to-peak separations, indicating superior enantioselectivity. Such modified HNTs achieve differentiation of about 600 mV, significantly higher than other methods already explored in literature, highlighting their efficient enantiorecognition [19,42–45]. Conversely, approaches based on current intensity differences, such as those using gold nano dendrites, M/P-SWCNTs, and cyclodextrin functionalized graphene derivatives, typically show a relative enantioselection between probe enantiomers (calculated as the ratio between current values of D- and L-analytes) [46–48]. As a matter of fact, current intensity-based methods do not allow for determining enantiomeric excess.

To complement the electrochemical characterization and provide a more comprehensive understanding of the system's behavior, the encapsulation efficiency (EE) and drug loading (DL) of DOPA into the HNTs were also determined (Fig. S8 (A)). The encapsulation efficiency was found to be 96 %, and the drug loading was 36 %. These values suggest that HNTs can effectively load DOPA, which is consistent with their reported potential as drug carriers. However, it is important to emphasize that the primary focus of this study is the demonstration of enantioselective recognition using HNT-based electrodes. The significant peak-to-peak separation observed in the voltammetric signals (Fig. 4) provides direct evidence of the system's ability to discriminate between D- and L-DOPA, highlighting its enantioselective recognition capabilities. While the high EE and DL values support the potential of HNTs for drug delivery, they are presented here to provide additional context and are secondary to the main objective of demonstrating and understanding the fundamental process of chiral discrimination at the electrode surface.

To further explore the potential of this system for controlled drug release, we investigated the release profiles of D- and L-DOPA from the HNTs. Based on a first-order release model, we have observed a differential release of the enantiomers, with D-DOPA exhibiting a faster release rate ($k = 0.15\ h^{-1}$) compared to L-DOPA ($k = 0.05\ h^{-1}$). This enantioselective release, illustrated in Fig. S8 (B), suggests that the chiral environment provided by the oligomer-modified HNTs could be exploited to control the release of individual enantiomers. It is crucial to note that these release profiles require further experimental validation to confirm their accuracy [49,50].

3.1. Challenges and future perspectives

While this study demonstrates the promising potential of HNT-based modified electrodes for enantioselective recognition, there are still some challenges that warrant attention. The limit of detection (LOD) of the HNTs-based modified electrode, while showing good sensitivity for DOPA detection, is higher than the LODs reported for most other electrochemical methods. This suggests that further optimization is needed to enhance the sensitivity of the method. Additionally, future

investigations should include a thorough assessment of the long-term stability and reusability of the modified electrodes, which are critical parameters for practical applications. The selectivity of the electrodes in complex matrices, beyond the demonstrated enantioselectivity for DOPA, also requires further evaluation. To gain a deeper understanding, future studies should also focus on elucidating the precise mechanism of enantiorecognition at the molecular level, potentially employing molecular modeling and simulation techniques.

Despite these challenges, the utilization of HNTs as a support for chiral selectors presents significant opportunities for the development of advanced enantioselective materials. Future research directions may include expanding the range of detectable chiral molecules to compounds of pharmaceutical, environmental, or industrial relevance, and developing HNT-based devices for enantioseparation. Furthermore, integrating HNT-based sensors into microfluidic systems could pave the way for miniaturized and automated enantioselective analysis. Exploring alternative surface modification strategies to optimize enantioselectivity and sensitivity is another promising avenue.

4. Conclusion

This study unveils a groundbreaking application of HNTs as a platform for bulk enantiorecognition. By chemically grafting inherently chiral oligomers onto the HNTs surface, we have created a novel electroactive substrate capable of bulk enantiorecognition. This innovative approach, confirmed through optical, spectroscopic, and thermal analyses, paves the way for designing advanced materials with tunable enantioselective properties. Our findings demonstrate the remarkable potential of these modified HNTs for enantioselective discrimination, exemplified by the impressive peak-to-peak separation achieved with DOPA enantiomers as model analytes (about 600 mV). While the high encapsulation efficiency and drug loading observed for DOPA, along with enantioselective release profiles, suggest potential utility in chiral drug delivery systems, the key contribution of this work remains the successful development of an HNT-based platform for enantioselective recognition, as evidenced by the distinct voltammetric responses to D- and L-DOPA. This breakthrough opens exciting possibilities for diverse applications, including electroanalysis, enantioseparation, and asymmetric synthesis, promising to revolutionize how we approach chiral molecules in various fields.

CRediT authorship contribution statement

Malinee Niamlaem: Writing – review & editing, Writing – original draft, Validation, Methodology, Investigation, Data curation. **Sara Grecchi:** Methodology, Investigation. **Punjapol Matthayom:** Methodology. **Chompunuch Warakulwit:** Writing – review & editing, Resources. **Daniela Maggioni:** Methodology. **Serena Arnaboldi:** Writing – review & editing, Supervision, Resources, Project administration, Funding acquisition, Conceptualization.

Declaration of competing interest

The authors declare that they have no known competing financial interests or personal relationships that could have appeared to influence the work reported in this paper.

Acknowledgments

This work has been funded by the European Research Council (ERC) under the HORIZON-ERC-2021 work program (grant agreement no 101040798, ERC Starting grant CHEIR).

The authors acknowledge Prof. T. Benincori, Prof. E. Licandro, Prof. S. Riela, Dr. G. Salinas and D. Fumagalli for fruitful discussions.

Nuclear Magnetic Resonance analyses were performed at the NMR facility of the Unitech COSPECT at the University of Milan (Italy).

Appendix A. Supplementary data

Supplementary data to this article can be found online at https://doi.org/10.1016/j.talanta.2025.128273.

Data availability

Data will be made available on request.

References

[1] S. Felletti, N. Marchetti, C. De Luca, M. Catani, C. Nosengo, G. Compagnin, D. Bozza, F.A. Franchina, L. Pasti, A. Cavazzini, Recent developments and future perspectives of chiral liquid chromatography for food safety and quality, TrAC, Trends Anal. Chem. 176 (2024) 117740, https://doi.org/10.1016/j.trac.2024.117740.

[2] J. Liu, H. Zhou, W. Yang, K. Ariga, Soft nanoarchitectonics for enantioselective biosensing, Acc. Chem. Res. 53 (3) (2020) 644–653, https://doi.org/10.1021/acs.accounts.9b00612.

[3] R.U. McVicker, N.M. O'Boyle, Chirality of new drug approvals (2013–2022): trends and perspectives, J. Med. Chem. 67 (4) (2024) 2305–2320, https://doi.org/10.1021/acs.jmedchem.3c02239.

[4] T.J. Ward, K.D. Ward, Chiral separations: a review of current topics and trends, Anal. Chem. 84 (2) (2012) 626–635, https://doi.org/10.1021/ac202892w.

[5] H.-L. Qian, S.-T. Xu, X.-P. Yan, Recent advances in separation and analysis of chiral compounds, Anal. Chem. 95 (1) (2023) 304–318, https://doi.org/10.1021/acs.analchem.2c04371.

[6] D. Wu, C. Ma, G.-C. Fan, F. Pan, Y. Tao, Y. Kong, Recent advances of the ionic chiral selectors for chiral resolution by chromatography, spectroscopy, and electrochemistry, J. Separ. Sci. 45 (1) (2022) 325–337, https://doi.org/10.1002/jssc.202100334.

[7] G. Salinas, M. Niamlaem, A. Kuhn, S. Arnaboldi, Recent advances in electrochemical transduction of chiral information, Curr. Opin. Colloid Interface Sci. 61 (2022) 101626, https://doi.org/10.1016/j.cocis.2022.101626.

[8] J. Muñoz, E. Redondo, M. Pumera, Chiral 3D-printed bioelectrodes, Adv. Funct. Mater. 31 (16) (2021) 2010608, https://doi.org/10.1002/adfm.202010608.

[9] S. He, X. Shang, W. Lu, Y. Tian, Z. Xu, W. Zhang, Electrochemical enantioselective sensor for effective recognition of tryptophan isomers based on chiral polyaniline twisted nanoribbon, Anal. Chim. Acta 1147 (2021) 155–164, https://doi.org/10.1016/j.aca.2020.12.058.

[10] V. Nagarajan, B. Arumugam, J. Annaraj, S.K. Ramaraj, Design of rutile nanospheres decorated rGO/β-CD nanoflakes composite: a sustainable electrocatalyst for effective non-enzymatic determination of L-Tyrosine, Sensor. Actuator. B Chem. 351 (2022) 130955, https://doi.org/10.1016/j.snb.2021.130955.

[11] R. Zilberg, Y. Teres, M. Agliulin, I. Vakulin, E. Bulysheva, M. Sycheva, V. Maistrenko, Chiral voltammetric sensor on the basis of nanosized MFI zeolite for recognition and determination of tryptophan enantiomers, Electroanalysis 36 (5) (2024) e202300375, https://doi.org/10.1002/elan.202300375.

[12] S.S. Upadhyay, N.S. Gadhari, A.K. Srivastava, Biomimetic sensor for ethambutol employing β-cyclodextrin mediated chiral copper metal organic framework and carbon nanofibers modified glassy carbon electrode, Biosens. Bioelectron. 165 (2020) 112397, https://doi.org/10.1016/j.bios.2020.112397.

[13] X. Niu, S. Yan, J. Chen, H. Li, K. Wang, Enantioselective recognition of L/D-amino acids in the chiral nanochannels of a metal-organic framework, Electrochim. Acta 405 (2022) 139809, https://doi.org/10.1016/j.electacta.2021.139809.

[14] X. Wei, L. Li, H. Lian, X. Cao, B. Liu, Grain-like chiral metal-organic framework/multi-walled carbon nanotube composited electrosensing interface for enantiorecognition of tryptophan, J. Electroanal. Chem. 886 (2021) 115108, https://doi.org/10.1016/j.jelechem.2021.115108.

[15] S. Assavapanumat, M. Ketkaew, A. Kuhn, C. Wattanakit, Synthesis, characterization, and electrochemical applications of chiral imprinted mesoporous Ni surfaces, J. Am. Chem. Soc. 141 (47) (2019) 18870–18876, https://doi.org/10.1021/jacs.9b10507.

[16] M. Niamlaem, S. Grecchi, F. Malacarne, G. Salinas, S. Arnaboldi, Enantioselective discrimination via wireless chemiresistive devices, ChemPlusChem (2024) e202400310, https://doi.org/10.1002/cplu.202400310.

[17] S. Grecchi, S. Arnaboldi, M. Korb, R. Cirilli, S. Araneo, V. Guglielmi, G. Tomboni, M. Magni, T. Benincori, H. Lang, P.R. Mussini, Widening the scope of "Inherently Chiral" electrodes: enantiodiscrimination of chiral electroactive probes with planar stereogenicity, Chemelectrochem 7 (16) (2020) 3429–3438, https://doi.org/10.1002/celc.202000657.

[18] S. Arnaboldi, S. Cauteruccio, S. Grecchi, T. Benincori, M. Marcaccio, A.O. Biroli, G. Longhi, E. Licandro, P.R. Mussini, Thiahelicene-based inherently chiral films for enantioselective electroanalysis, Chem. Sci. 10 (5) (2019) 1539–1548, https://doi.org/10.1039/C8SC03337D.

[19] S. Arnaboldi, T. Benincori, R. Cirilli, S. Grecchi, L. Santagostini, F. Sannicolò, P. R. Mussini, "Inherently chiral" thiophene-based electrodes at work: a screening of enantioselection ability toward a series of pharmaceutically relevant phenolic or catecholic amino acids, amino esters, and amine, Anal. Bioanal. Chem. 408 (26) (2016) 7243–7254, https://doi.org/10.1007/s00216-016-9852-x.

[20] D. Jiang, H. Jing, Z. Liu, C. Jia, Q. Liu, Natural halloysite nanotube as a spatially confined nanoreactor for improving photocatalytic performance, J. Phys. Chem. C 125 (28) (2021) 15316–15323, https://doi.org/10.1021/acs.jpcc.1c04065.

[21] Y. Lvov, W. Wang, L. Zhang, R. Fakhrullin, Halloysite clay nanotubes for loading and sustained release of functional compounds, Adv. Mater. 28 (6) (2016) 1227–1250, https://doi.org/10.1002/adma.201502341.
[22] Y. Feng, X. Chen, R.-R. He, Z. Liu, Y.M. Lvov, M. Liu, The Horizons of medical mineralogy: structure-bioactivity relationship and biomedical applications of halloysite nanoclay, ACS Nano 18 (31) (2024) 20001–20026, https://doi.org/10.1021/acsnano.4c04372.
[23] P. Zhao, Y. Feng, Y. Zhou, C. Tan, M. Liu, Gold@Halloysite nanotubes-chitin composite hydrogel with antibacterial and hemostatic activity for wound healing, Bioact. Mater. 20 (2023) 355–367, https://doi.org/10.1016/j.bioactmat.2022.05.035.
[24] J. Wang, Y. Zhang, J. Si, W. Zhang, Q. Liang, W. Li, B. Jin, S. Miao, Structural engineering of NiFe-Layered double hydroxides and halloysite composites for efficient CO_2 capture, Chem. Eng. J. 463 (2023) 142502, https://doi.org/10.1016/j.cej.2023.142502.
[25] M. Al-abidy, A. Al-nayili, Enhancement of photocatalytic activities of $ZnFe_2O_4$ composite by incorporating halloysite nanotubes for effective elimination of aqueous organic pollutants, Environ. Monit. Assess. 195 (1) (2022) 190, https://doi.org/10.1007/s10661-022-10811-4.
[26] F. Tao, X. Wang, S. Jin, L. Tian, Z. Liu, X. Kang, Z. Liu, A composite of hierarchical porous MOFs and halloysite nanotubes as single-ion-conducting electrolyte toward high-performance solid-state lithium-ion batteries, Adv. Mater. 35 (29) (2023) 2300687, https://doi.org/10.1002/adma.202300687.
[27] F. Malacarne, S. Grecchi, M. Niamlaem, B. Bonczak, G. Salinas, S. Arnaboldi, Unconventional approaches for chiral resolution, Anal. Bioanal. Chem. 416 (16) (2024) 3677–3685, https://doi.org/10.1007/s00216-024-05329-2.
[28] S. Grecchi, F. Malacarne, R. Cirilli, M. Dell'Edera, S. Ghirardi, T. Benincori, S. Arnaboldi, Wireless hollow miniaturized objects for electroassisted chiral resolution, Anal. Chem. 96 (12) (2024) 4901–4908, https://doi.org/10.1021/acs.analchem.3c05544.
[29] S. Grecchi, B. Bonczak, F. Malacarne, G. Salinas, R. Cirilli, S. Arnaboldi, Wireless asymmetric umpolung electrosynthesis, Chem. Commun. 60 (74) (2024) 10120–10123, https://doi.org/10.1039/D4CC02406K.
[30] S. Butcha, S. Assavapanumat, S. Ittisanronnachai, V. Lapeyre, C. Wattanakit, A. Kuhn, Nanoengineered chiral Pt-Ir alloys for high-performance enantioselective electrosynthesis, Nat. Commun. 12 (1) (2021) 1314, https://doi.org/10.1038/s41467-021-21603-8.
[31] X. Huang, Q. Zhang, J. Lin, K. Harms, E. Meggers, Electricity-driven asymmetric lewis acid catalysis, Nat. Catal. 2 (1) (2019) 34–40, https://doi.org/10.1038/s41929-018-0198-y.
[32] F. Sannicolò, S. Arnaboldi, T. Benincori, V. Bonometti, R. Cirilli, L. Dunsch, W. Kutner, G. Longhi, P.R. Mussini, M. Panigati, M. Pierini, S. Rizzo, Potential-driven chirality manifestations and impressive enantioselectivity by inherently chiral electroactive organic films, Angew. Chem. Int. Ed. 53 (10) (2014) 2623–2627, https://doi.org/10.1002/anie.201309585.
[33] J. Heinze, B.A. Frontana-Uribe, S. Ludwigs, Electrochemistry of conducting polymers—persistent models and new concepts, Chem. Rev. 110 (8) (2010) 4724–4771, https://doi.org/10.1021/cr900226k.
[34] J.G. Ibanez, M.E. Rincón, S. Gutierrez-Granados, M.h. Chahma, O.A. Jaramillo-Quintero, B.A. Frontana-Uribe, Conducting polymers in the fields of energy, environmental remediation, and chemical–chiral sensors, Chem. Rev. 118 (9) (2018) 4731–4816, https://doi.org/10.1021/acs.chemrev.7b00482.
[35] B. Liu, X. Lin, P. Zhao, Y. He, M. Liu, Robust polypyrrole@halloysite nanotube-coated polyurethane sponge as multifunctional flexible sensors, ACS Sustain. Chem. Eng. 11 (24) (2023) 8753–8763, https://doi.org/10.1021/acssuschemeng.2c07370.
[36] A. Khan, A. Hassanein, S. Habib, M. Nawaz, R.A. Shakoor, R. Kahraman, Hybrid halloysite nanotubes as smart carriers for corrosion protection, ACS Appl. Mater. Interfaces 12 (33) (2020) 37571–37584, https://doi.org/10.1021/acsami.0c08953.
[37] C. Dong, M. Zhang, T. Xiang, L. Yang, W. Chan, C. Li, Novel self-healing anticorrosion coating based on L-valine and MBT-loaded halloysite nanotubes, J. Mater. Sci. 53 (10) (2018) 7793–7808, https://doi.org/10.1007/s10853-018-2046-5.
[38] A. Qureshi, S. Habib, M. Nawaz, R.A. Shakoor, R. Kahraman, E.M. Ahmed, Modified halloysite nanotubes decorated with ceria for synergistic corrosion inhibition of polyolefin based smart composite coatings, Appl. Clay Sci. 233 (2023) 106827, https://doi.org/10.1016/j.clay.2023.106827.
[39] C. Chao, J. Liu, J. Wang, Y. Zhang, B. Zhang, Y. Zhang, X. Xiang, R. Chen, Surface modification of halloysite nanotubes with dopamine for enzyme immobilization, ACS Appl. Mater. Interfaces 5 (21) (2013) 10559–10564, https://doi.org/10.1021/am4022973.
[40] S. Arnaboldi, D. Vigo, M. Longhi, F. Orsini, S. Riva, S. Grecchi, E. Giacovelli, V. Guglielmi, R. Cirilli, G. Longhi, G. Mazzeo, T. Benincori, P.R. Mussini, Self-standing membranes consisting of inherently chiral electroactive oligomers: electrosynthesis, characterization and preliminary tests in potentiometric setups, Chemelectrochem 6 (16) (2019) 4204–4214, https://doi.org/10.1002/celc.201900779.
[41] W. On Yah, A. Takahara, Y.M. Lvov, Selective modification of halloysite lumen with octadecylphosphonic acid: new inorganic tubular micelle, J. Am. Chem. Soc. 134 (2012) 1853–1859, https://doi.org/10.1021/ja210258y.
[42] H. Lian, S. Huang, X. Wei, J. Guo, X. Sun, B. Liu, Gold nanodendrite-based differential potential ratiometric sensing strategy for enantioselective recognition of DOPA, Talanta 210 (2020) 120654, https://doi.org/10.1016/j.talanta.2019.120654.
[43] T. Nakanishi, M. Matsunaga, M. Nagasaka, T. Asahi, T. Osaka, Enantioselectivity of redox reaction of DOPA at the Gold electrode modified with a self-assembled monolayer of homocysteine, J. Am. Chem. Soc. 128 (41) (2006) 13322–13323, https://doi.org/10.1021/ja062380f.
[44] S. Ates, E. Zor, I. Akin, H. Bingol, S. Alpaydin, E.G. Akgemci, Discriminative sensing of DOPA enantiomers by cyclodextrin anchored graphene nanohybrids, Anal. Chim. Acta 970 (2017) 30–37, https://doi.org/10.1016/j.aca.2017.03.052.
[45] S. Arnaboldi, G. Salinas, G. Bonetti, R. Cirilli, T. Benincori, A. Kuhn, Bipolar electrochemical measurement of enantiomeric excess with inherently chiral polymer actuators, ACS Meas. Au 1 (3) (2021) 110–116, https://doi.org/10.1021/acsmeasuresciau.1c00011.
[46] W. Kuang, H. Luo, Z. Zhu, Exploring the potential of inherent chiral single-walled carbon nanotubes in enantioselective electrochemical sensing: a novel microsensor for discriminating DOPA enantiomers, Electrochim. Acta 487 (2024) 144162, https://doi.org/10.1016/j.electacta.2024.144162.
[47] Y. Chen, J. Xu, C. Chen, D. Guo, Y. Fu, The application of L-tryptophan functionalized graphene-supported platinum nanoparticles for chiral recognition of DOPA enantiomers, New J. Chem. 39 (2015) 6919–6924, https://doi.org/10.1039/C5NJ00303B.
[48] J. Kou, Z. Zhu, J. Jiang, L. Chen, K. Zhang, G. Shan, X. Wang, Z. Su, C. Sun, A porous aromatic cage-based electrochemical sensor for enantioselective recognition of DOPA, Chem. Commun. 60 (2024) 6949–6952, https://doi.org/10.1039/D4CC02622E.
[49] M. Parkash, M.H. Shoaib, M. Sikandar, R.I. Yousuf, M.T. Saleem, F.R. Ahmed, F. Siddiqui, Formulation development, characterization, and mechanistic PBPK modeling of metoclopramide loaded halloysite nanotube (HNT) based drug-in-adhesive type transdermal drug delivery system, Sci. Rep. 14 (2024) 28512, https://doi.org/10.1038/s41598-024-80089-8.
[50] Y.M. Lvov, M.M. DeVilliers, R.F. Fakhrullin, The application of halloysite tubule nanoclay in drug delivery, Expet Opin. Drug Deliv. 13 (2016) 977–986, https://doi.org/10.1517/17425247.2016.1169271.